

CHAPTER V

BUILDING OF THE ULTRACENTRIFUGE

1. Introduction.

It was the aim of the present aether drift experiment to achieve as high a potential accuracy as possible. For that reason, a rotor system had to be designed that allowed not only for an optimization but also a variation of the experimental parameters so that the systematic errors could be minimized and their effects established.

For this experiment it was also essential to position the gamma ray detector at the center of the rotor so that a high efficiency cycle could be obtained and the rotor frequency be used to spatially modulate the $\underline{U} \cdot \underline{V}$ term (in Equation 4.3.3) and make any angular dependencies of the counting rate directly apparent.

To allow for such a geometry the rotor axis had to be stable to within 0.05 mm over periods of several weeks. This requirement eliminated the possibility of spinning the rotor on a glass plate, a technique that has been used previously in this laboratory (Marshall et al., 1948). The operation of such a rotor was found to be unreliable as the ball bearings had to be replaced daily and the position could vary by as much as 1 cm. Similarly a bearing suspension was not satisfactory as it would have created excessive vibrations and would not have provided the necessary positioning of the rotor.

To obtain the stabilities needed it was thus necessary to build a free magnetic suspension as has been used by Beams (1951). This in turn raised the problem of the

BASIC ROTOR STRUCTURE

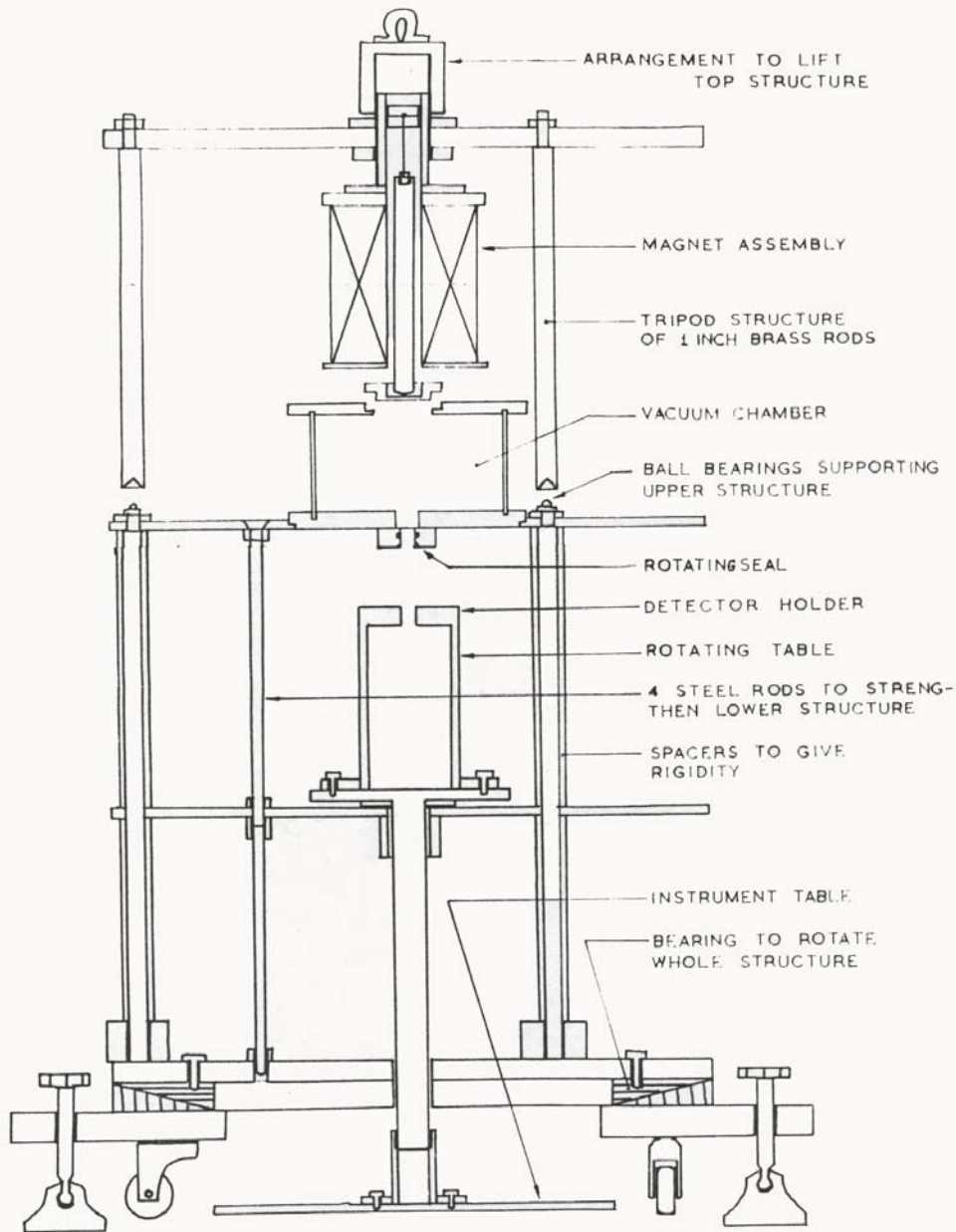


FIGURE 5.1

acceleration and damping of the rotor. The detector had to be positioned at the lower axis of the rotor so that it was not possible to accelerate the rotor mechanically, as was done by Beams using an air turbine. In order to critically damp the horizontal motion of the rotor and to position it externally a different damping mechanism had also to be built.

Preliminary tests using small rotors showed that the rotor stability was greatly determined by the rigidity of the structure so that this became a major consideration in designing the apparatus.

2. Rotor Structure.

In Figure 5.1 and Plate 5.1 the details of the structure are shown. The scale of the assembly was determined by the size of the largest rotor used and the general lay out was designed to make access to the various parts and especially the vacuum chamber easy.

Five levels of instrumentation are supported by the tripod structure, the top part of which can be lifted off by a hoist arrangement. The lower part is further strengthened by four adjustable steel rods and three brass sleeves fitted over the 1" brass rods. The sleeves also act as spacers for three of the platforms.

The various platforms have distinct functions. The top plate supports the electromagnet and a periscope, which allows a remote monitoring of the rotor. Plate 2 positions the vacuum chamber, the optics for the suspension servo mechanism, and two steel safety barricades. The diffusion pump and cooling baffle are mounted onto Plate 3, which also supports the rotating instrumentation table. Plate 4 is mounted onto a large bearing so that the whole structure can be turned remotely. It also positions the motors, which rotate the instrumentation table and the structure as a whole.

Plate 5 is part of the instrumentation table and supports the electronics for the proportional counter, which in turn is clamped to the upper part of the table and is positioned by the rotating seal at the lower part of the vacuum chamber.

The whole structure can also be moved about and leveled using castors and adjustable legs. This general design proved to be very reliable. The structure has no appreciable resonance frequencies to interfere with the rotor operation.

ROTOR AS SUSPENDED

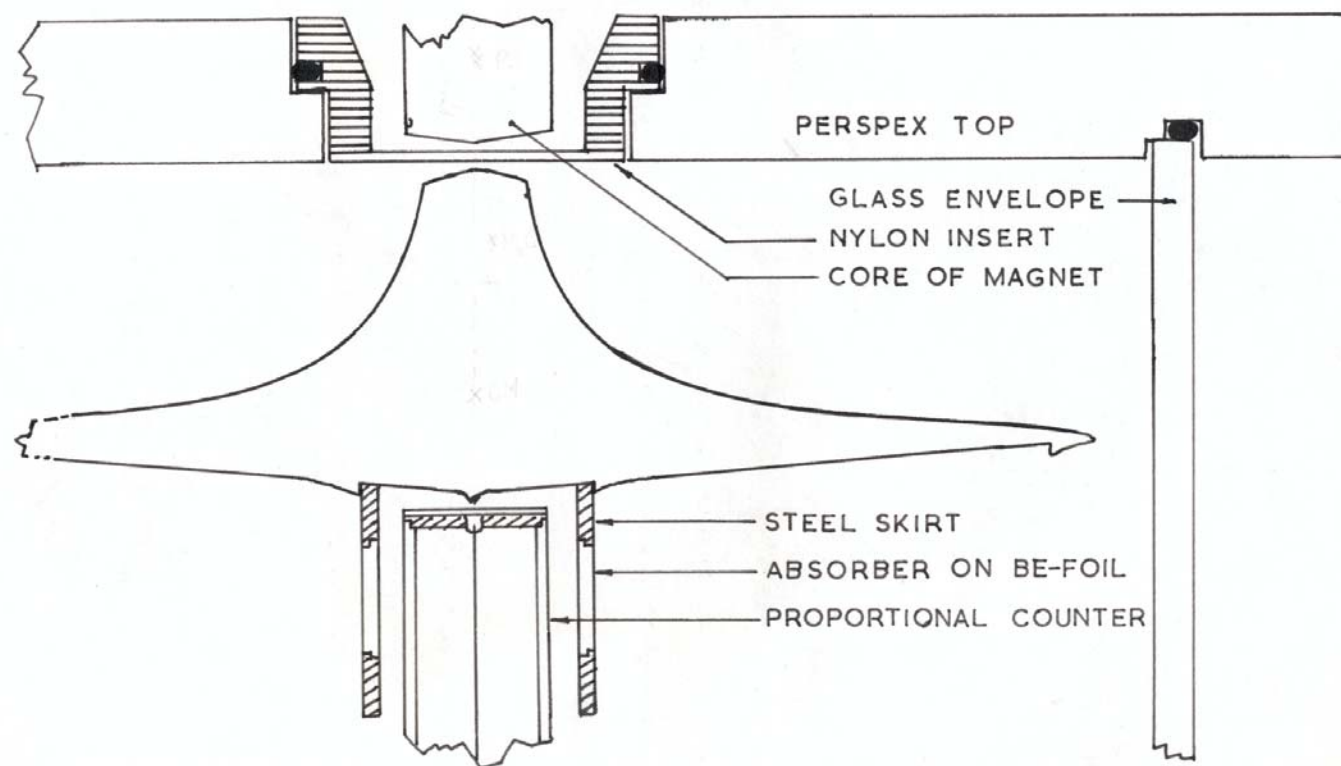


FIGURE 5.2

3. Magnetic Suspension.

The basic design of the magnetic suspension followed that of Beams and is shown in Figures 5.2, 5.3 and Plate 5.2. The current in the electromagnet is controlled by a servo-loop, the control signal for which is derived from an optical network, which determines the vertical position of the rotor.

3.1 General Considerations.

Because of the complex shape of the rotor it is not possible to calculate exactly the fields necessary to suspend the large rotor (2.7 kg). It is possible, however, to make some general comments, which help one to understand the characteristics of the magnetic suspension.

Let r be the distance between the lower part of the core and the tip of the rotor, and L the length of the core. If $r \ll L$, one can then regard the magnetic dipole moment of the core as consisting of two magnetic monopoles $\pm Q_m$ (Hallen, 1962) separated by a distance L^1 and of magnitude

$$Q_m = \frac{iNS}{L^1}$$

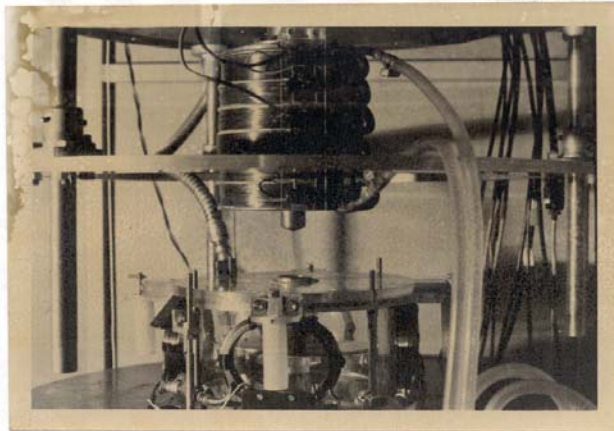


PLATE 5.2. Top part of rotor structure before assembling.

where i is the current and N the number of turns of the electromagnet. S is the cross section of the core and $L^1 \approx L - 2r_1$, where r_1 is the distance of Q_m from the tip of the core. The flux density below the core is then given by

$$|B(r)| = \frac{\mu_0 Q_m}{4\pi(r_1 + r)^2}$$

where μ_0 is the primary magnetic constant. r_1 can be found by measuring $B(r)$ as a function of r and is 1.7 cm for the particular core geometry used.

Similarly one can think of the magnetic dipole moment of the rotor as consisting of two poles $\pm Q_m^1$, one located a distance r_2 (~ 1 cm) below the top of the rotor and the other at its rim. This approximation is not as good as before but suffices for the present purpose. The problem of the magnetic suspension is then reduced to one involving a 'simple' pendulum of length $(r_1 + r_2 + r)$.

To calculate the induced magnetic dipole moment of the rotor, one would have to know how the magnetic flux density becomes altered in the presence of the rotor, and how the permeability of the rotor depends on $|B(r)|$ and the exact shape of the rotor.

These factors are not easily calculated. However, taking a small volume element Δn in the top part of the rotor, one can assume that the permeability over that region is constant, i.e., $B = \mu_0 \mu H = \mu_0 (\underline{H} + \underline{M})$, and that the induced magnetic moment $\Delta \underline{m}$ of that volume element does not significantly influence the magnetic flux density $B(r)$.

μ_0 and μ are the absolute and relative permeability respectively. The intensity of magnetization of that volume element is

$$\underline{M}(r) = \frac{\Delta \underline{m}}{\Delta n}$$

and the force on it

$$f = (M \cdot \tilde{N}) \underline{B} = (\mu - 1) \mu_0 \mu (H \cdot \tilde{N}) \underline{H}$$

which along the axis of suspension becomes

$$|f| = \frac{(\mu - 1) \mu_0 Q_m^2}{8\pi^2 \mu (r_1 + r_2 + r)^5} \quad \dots 3.1$$

As Q_m is proportional to the current in the electromagnet, one finds that in order to keep the force of attraction constant

$$i \propto (r_1 + r_2 + r)^{5/2}$$

This will still hold for the rotor as a whole as long as the range of the vertical displacements Δr considered satisfies

$$\Delta r \ll (r_1 + r_2 + r)$$

Equation 5.3.1 indicates that the force of attraction is proportional to i^2 and does not greatly depend on the relative permeability of the material as long as it is greater than 1. The force can also be increased by decreasing the distances r_1 and r_2 , i.e., by tapering the core and the top of the rotor as shown in Figure 5.2. This would also improve the suspension characteristics by providing a definite point-to-point suspension.

As the apparent permeability of the core is of the order of 30, the magnetic flux lines are virtually normal to the lower surface of the core. One can thus plot the flux line

ELECTROMAGNET ASSEMBLY

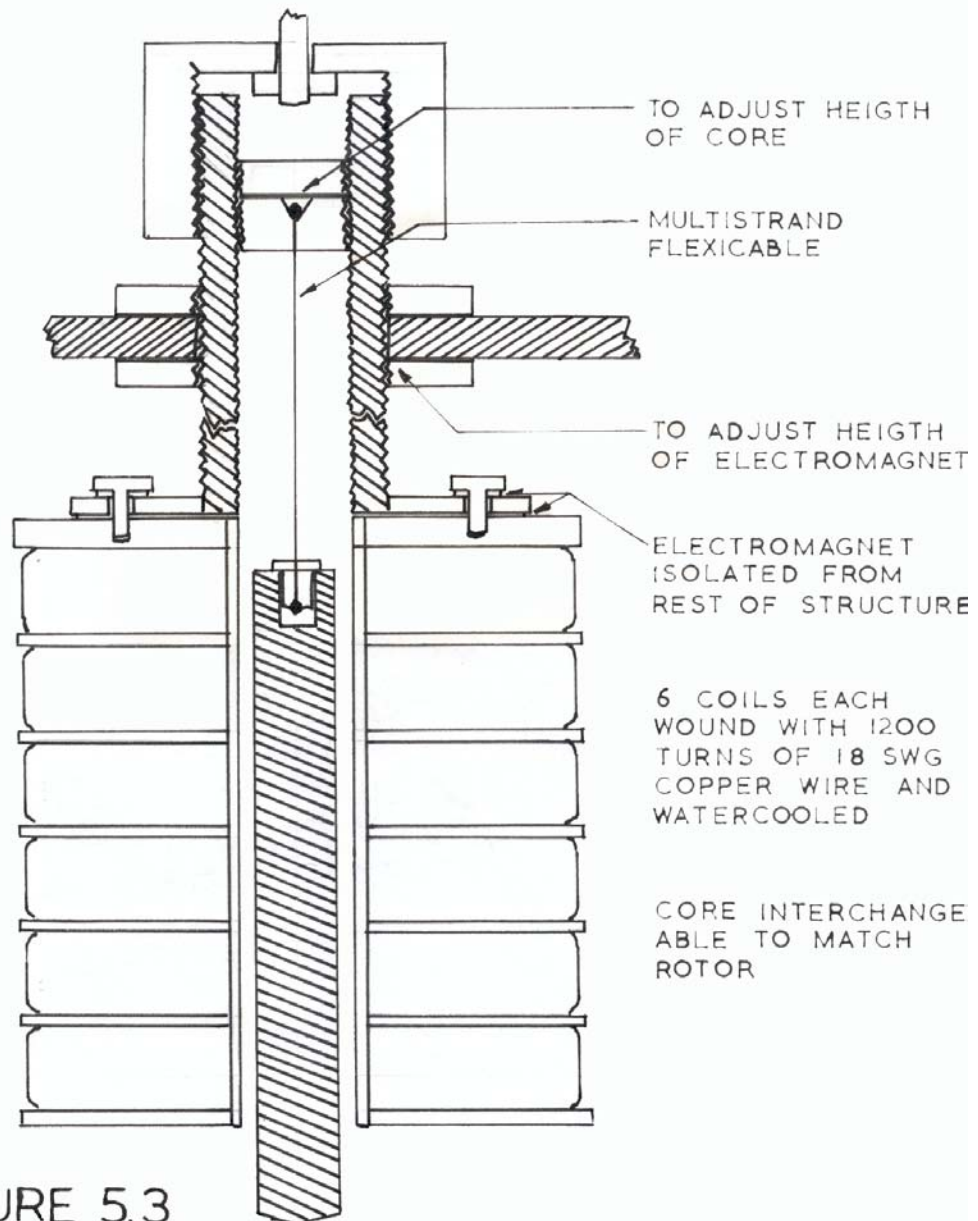


FIGURE 5.3

distribution and find the optimum taper of the core. It is a compromise between the above considerations and achieving the largest magnetic flux density at the rotor.

3.2 Core Material.

The core material had to have a small hysteresis and exhibit no magnetic saturation for the field strengths used. These requirements were, however, easily satisfied for $B \sim 500$ gauss, the maximum flux densities needed to suspend the rotor. The material used is sold under the trade name of 'Hellefors Remko magnetic iron', and is generally known as Swedish steel. It is composed of, C (.03%), Si (.01%), Mn (.12%), S (.01%), Cu (.01%) and iron, and has a maximum permeability of 10850. It is easy to work on and thus satisfied all criteria.

3.3 The Electromagnet.

The electromagnet (see Figure 5.3 and Plate 5.2) consists of 6 coils each containing 1200 turns of 18 SWG copper wire, with the various coils not only insulated from one another, but also from the structure as a whole as an added safety measure to prevent a direct short to earth. Each coil is water-cooled and can handle currents of up to 5 amps. Generally, however, only 1 amp is needed to keep the rotor suspended at a distance of $r=4$ mm.

Various means of adjustment were incorporated in the design of the magnet to allow a change in the magnet height and the position of the core, so that different cores can be installed depending on the size of the rotor used.

3.4 Suspension Serve Mechanism. The main problem then was to build a reliable suspension system, which depended on an accurate position sensor of the rotor and a stable electronic servo system.

Several sensors were considered and prototypes of a capacitive and an optical system with the respective servo systems were built. The capacitive sensor did measure the rotor position accurately, but it was also very sensitive to the general noise level of the laboratory, whereas the light-photocell sensor was comparatively insensitive to noise as the gain of the amplifier was smaller.

Plate 5.3 shows the design of the optical system. Two 1" prisms deflect the light from the lamp across the top of the rotor to the photocell. Both the light bulb and the photocell are mounted inside brass sleeves, which in turn are rigidly fastened to the brass plate supporting the vacuum chamber. This way the filament of the lamp is shielded from the rotating magnetic field used to accelerate the rotor, and the noise pick-up at the photocell is kept at a minimum. The collimating lenses and the prisms can be adjusted so as to keep the vertical position of the rotor constant over a range of horizontal displacements ($\sim 1\text{cm}$). Also the height of the light bulb and the photocell can be adjusted to ensure a smooth lifting action of the rotor and a linear control over its height.

For these reasons the optical system was superior to the capacitive position sensor, even though the former was potentially less reliable, as it depended on the finite lifetime of the lamp filament (see next section).

The schematic of the suspension servo system is shown in Figure 5.4. The output of the photocell is amplified by a high gain integrated operational amplifier (type $\mu\text{A } 709$, supplied by the courtesy of Fairchild Inc., U.S.A.), which has an open loop gain of 65000 and a temperature coefficient of $3.0 \mu\text{V}/^\circ\text{C}$. The output of the amplifier drives the power amplifier of an emitter follower type. A voltage feedback signal via resistor R_4 decreases the signal noise on the output current by a factor of 30 to less than 10 mV.



PLATE 5.3. Rotor with steel skirt and optics

SUSPENSION SYSTEM

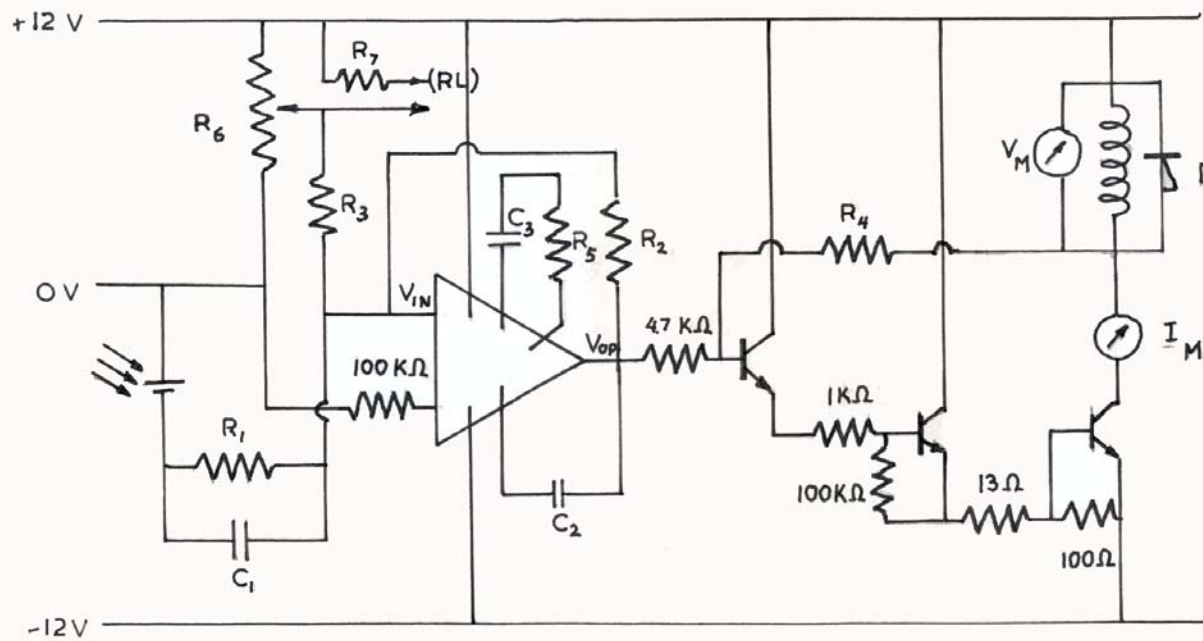


FIGURE 5.4

The output of the power amplifier drives the electromagnet L, which is protected by diode D against sudden voltage surges. The power for the suspension system is supplied by two stabilized 12-volt power supplies, which in turn are powered by two 18-volt accumulators to make the suspension system independent of the Midland Electricity Board. The accumulators were continuously trickle charged and in case of an electricity failure they would have provided enough power for 15 hours. Before installing the 2 voltage stabilizing networks, the ripple on the supply voltage was about 300 mV and the voltage depended strongly on the charging rate of the accumulators. The stabilizing networks reduced the ripple to 5 mV and made the output supply voltage constant over a 2 volt range of the accumulator voltages.

The most difficult problem in designing the suspension servo loop was to find the correct feedback values to critically damp the vertical motion of the rotor. These had to be found empirically, as it was not possible to obtain a Nyquist diagram, i.e., the transfer function between input and output signal, until the rotor was suspended, as it was an integral part of the feedback system. To suspend the rotor, however, one had to know the transfer function. In retrospect, it should be said that it would have been helpful to measure the transfer function even without the rotor in order to determine the frequency response of the suspension system. Figure 5.5 is the Nyquist diagram of the system with the final feedback values. It shows that the maximum gain of 7,750 occurs for a frequency of 245 cps and that the cut-off frequency is around 10,000 cps with a negligible amount of positive feedback at 150,000 cps.

NYQUIST DIAGRAM

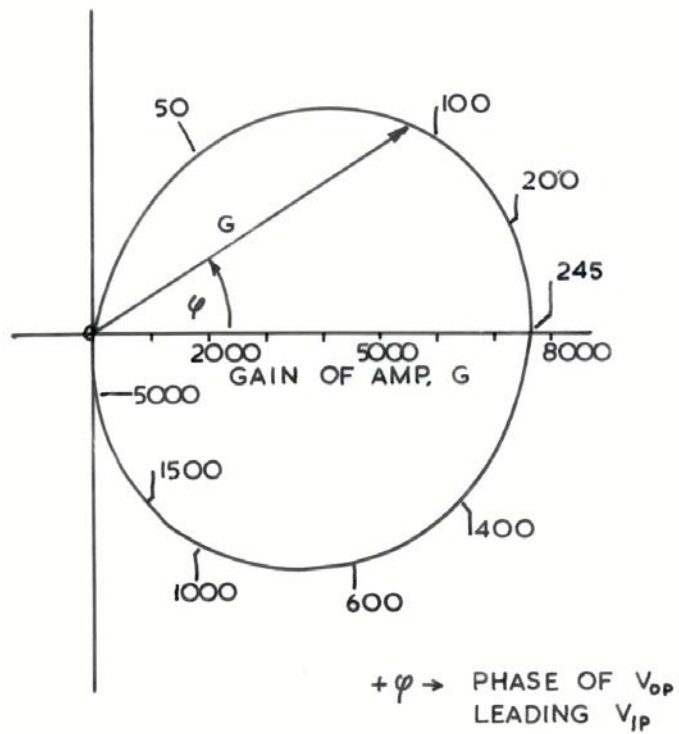


FIGURE 5.5

A damping of the vertical motion of the rotor was achieved by adding capacitor C_1 in parallel with the input resistor R_1 (100 k Ω). Critical damping was obtained by choosing $C_1 = 0.25 \mu\text{F}$, but a slightly higher value was used (.35 μF) to make the system less sensitive to transients.

Resistor R_2 determines the gain of the amplifier, and components C_3 , R_5 , and C_2 limit the input and the output frequency range. Increasing C_3 from .001 μF to .005 μF decreased the response of the circuit at 2.5 kcs by a factor of 5 and made it less sensitive to noise pick-up. Varying C_2 had generally little effect on the characteristics of the suspension.

The lifting action of the circuit is controlled by the 100 k Ω helipot R_6 . To suspend the rotor, one merely has to increase the current in the electromagnet until the rotor is attracted, at which point the servo loop takes over. After the circuit has become temperature stabilized, it gives a remarkably constant current output, limited mainly by the fluctuations in the supply voltage and the light output from the lamp. The rotor has been run constantly for periods of over two weeks without major adjustments.

3.5 Filament Safety Features.

The lamp filament is the weakest link in the suspension system as its life time was rated at a 1000 hours. This, however, was effectively increased by a factor of 10 by reducing the supply voltage from the rated 24 volts to 21 volts (Specifications for W filaments, Menzel and Brandau, W. Germany). In addition, the lamp was regularly replaced every 1000 hours and then every new bulb was run in for 50 hours before accelerating the rotor to guard against a mechanical failure of the filament.

CURRENT SUPPLY FOR THE LAMPS

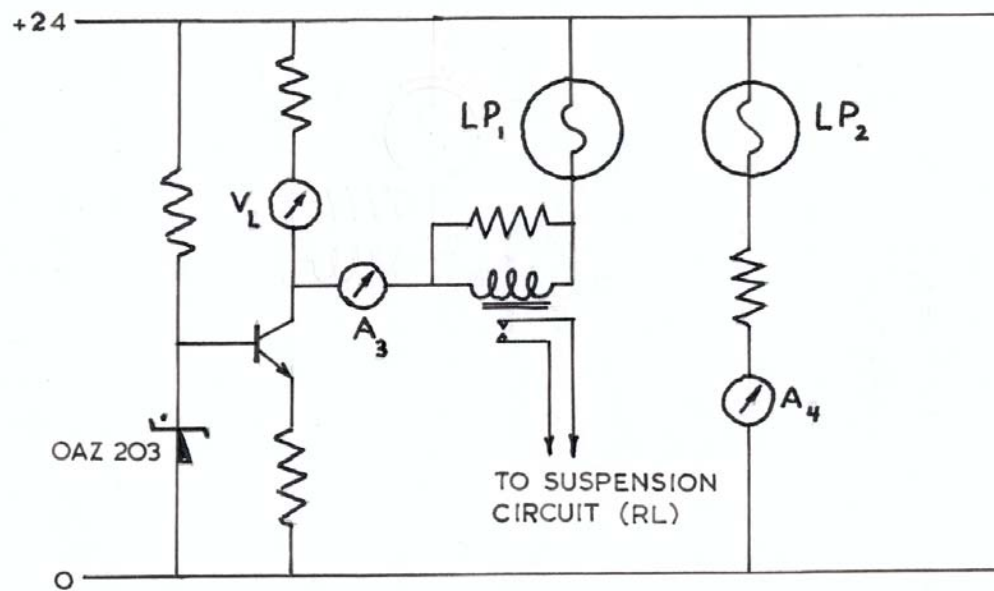


FIGURE 5.6

This, of course, did not eliminate the ever-present threat of a filament failure. So, as to reduce the likelihood of a breakdown, a relay (RL) was built into the lamp power supply (see Figures 5.4 and 5.6), which in case of a filament failure adjusted the current in the electromagnet so that 90% of the weight of the rotor was 'suspended.' The rotor then would hopefully continue to spin on an agate plate at the top of the proportional counter (see Figure 5.2). Fortunately, we never had to use this facility, so the author is unable to report on its reliability.

The finite resistance of the lamp contacts also made the suspension system less reliable, but this problem was overcome by actually soldering the lamp into the socket.

4. Monitoring the Operation of the Rotor.

As the rotor structure was enclosed in a cubicle, separate from the main laboratory, the operation of the rotor had to be remotely monitored. This was done visually by a periscope and a system of mirrors. It was generally found, however, that the meters, monitoring various aspects of the suspension system, and the oscilloscope trace of the control voltage V_{OP} (see Fig. 5.4) were more effective in displaying any irregularities in the rotor suspension.

At the control console the following parameters can be monitored:

- i) the voltage across the electromagnet V_m ,
- ii) the current supplied to the magnet I_m ,
- iii) the voltage supplied to the suspension lamp V_L ,
- iv) the current supplied to the suspension lamp I_{LL} ,
- v) the current supplied to the gating lamp (see section 6.5) I_{L2} ,

- vi) the supply voltage to the suspension system V_s ,
- vii) the charging rate and the accumulator voltage V_A .

The currents needed to suspend the rotor ranged from 1.8 amps to 3.2 amps, and in the later part of the experiment I_m was measured more accurately by using a voltage to frequency converter and a frequency counter.

5. Damping and Positioning of the Rotor.

In the aether drift experiment the vertical axis of the rotor had to be positioned to within .1 mm and held constant to better than .05 mm (see Fig. 5.2). The vertical motion of the rotor was also restricted to ± 1 mm, so that it became essential to not only position the rotor accurately but also damp its motion effectively.

The vertical motion could be damped electronically by choosing appropriate feed back values in the servo loop. The horizontal damping presented a more difficult problem, as it had to be done mechanically. As the rotor was accelerated it went through several resonances caused by the pendulum motion of the magnet core about its point of support, the pendulum motion of the rotor about its suspension point and the resultant action of this compound pendulum. Also, at 100 cps, a resonance was observed which was caused by the coupling of the horizontal and the vertical motion.

To damp these motions a central oil dash-pot damping of the core was found to be insufficient and the system, shown in Figure 5.7, was developed. This provided a strong damping and could also be used to position the core and the rotor. It had the advantage of allowing a number of extra parameters for the adjustment of the damping constants. The leaf springs were made of phosphor bronze. A thickness of 18 gauge made the

springs weak enough to follow the motion of the rotor, yet strong enough to position it accurately.

Various damping fluids were tried but epoxy resin (without hardener) was found to be the most effective. It gave a damping constant of 3 sec compared to 8 sec in air.

The tension and the position of the springs could be adjusted by locking nuts and two of the spring assemblies were movable so that the position of the rotor could be varied during a medium high speed run without disturbing the rotor.

POSITIONING AND DAMPING OF ROTOR

(IN HORIZONTAL PLANE)

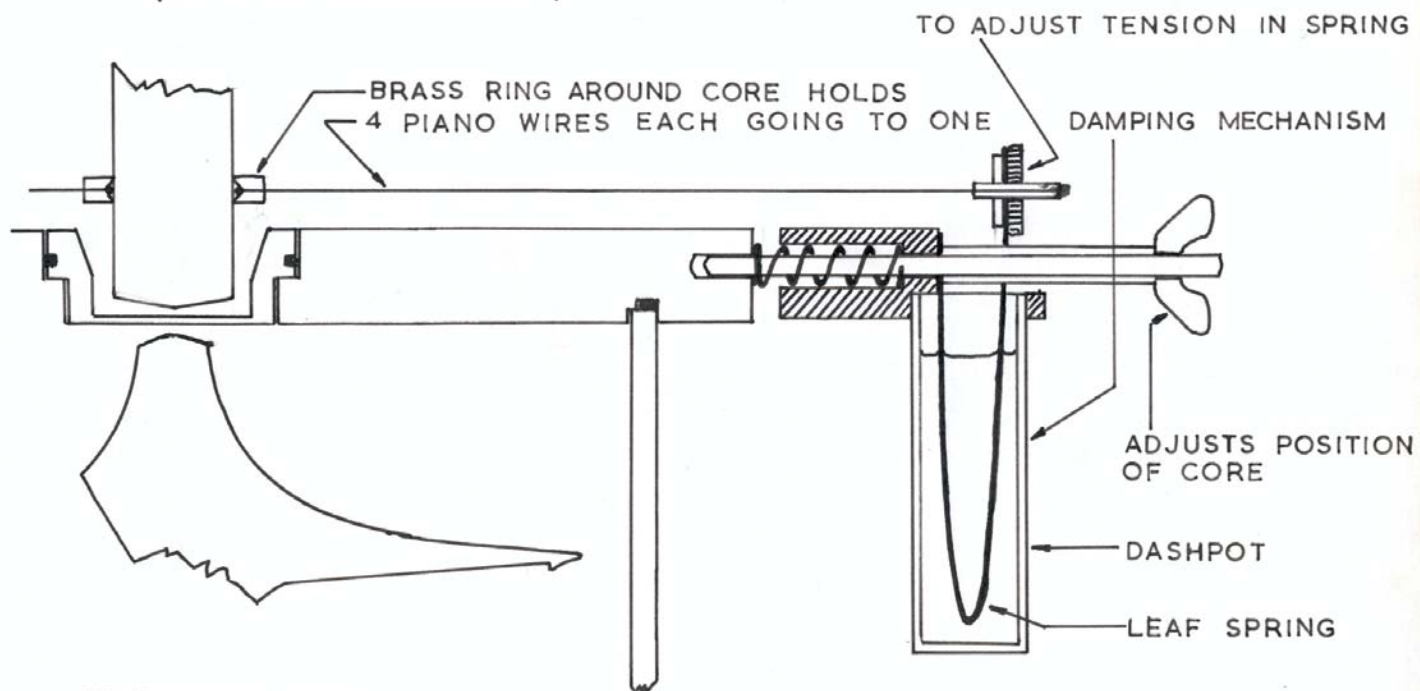


FIGURE 5.7

6. The Rotor.

As the sensitivity of the aether drift experiment is directly proportional to the tip speed ($V_s - V_a$) of the rotor, it became essential to optimize the shape of the rotor, while at the same time incorporating a number of features to allow for the mounting of the source and the absorber.

6.1 Shape.

The necessity of having a central detector eliminated the possibility of a hollow-rod-type rotor as it would not have had sufficient overall strength. For this and other reasons, the alternative of a disc-shaped rotor was preferable, as it can be directly machined on a profile lathe and is also less sensitive to imbalances. Figure 5.8 shows the final design.

CROSS-SECTION OF ROTOR

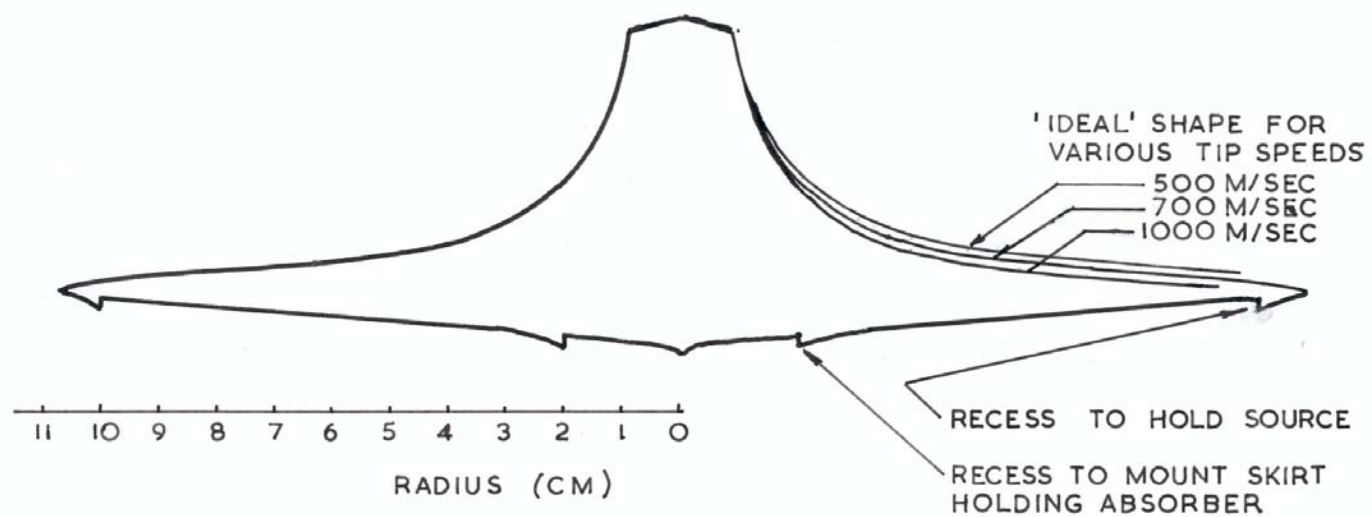


FIGURE 5.8

Marshall et al. (1948) have shown that in order to obtain an equal stress throughout the rotor, its profile would have to conform to a Gaussian error function with the thickness as a function of radius expressed by

$$t(r) = t_o \exp(-\omega^2 r^2 \rho / 2S)$$

where t_o is the thickness at the center of the rotor, S the tensile strength and ρ the density of the rotor material.

Figure 5.8 shows the ideal shape for various tip speeds, assuming a tensile strength of 125 tsi at .2% proof stress. Only the top surface could be approximated to this shape. The lower surface had to be made virtually flat, so that most of the radiation coming from the source, mounted at the rim of the rotor, could reach the detector. Towards the rim the angle of both surfaces was equal to produce as much of a uniform stress in that part of the rotor as possible. Two recesses were machined in the lower surface to hold the source and the absorber skirt. In the course of the experiment two different skirts were used. One consisted of a steel tube with a wall thickness of 2.5 mm and windows cut at opposite sides. This allowed the radiation to penetrate through the absorber foil, which was held in place by a .016" thick beryllium disc. The other skirt consisted of a beryllium tube of 2 mm wall thickness. The skirt was reamed into the inner recess of the rotor and then araldited into place.

The top of the rotor was determined by previous considerations (see section 5.3.1). A point at the lower axis of the rotor allowed it to spin on an agate plate in case of a filament failure. In order to test this rotor design a wax model was built and spun to breaking point. It showed, as was expected, that the rim of the rotor was the weakest point.

6.2 Rotor Material.

The material had to satisfy several criteria. It had to be ferromagnetic for the magnetic suspension. It had to have as high a ratio of $\frac{\text{tensile strength}}{\text{density}}$ as possible and at the same time it had to be soft enough to make machining possible.

These conditions were best satisfied by maraging steel, a relatively new steel-nickel-cobalt-molybdenum alloy*. The material exhibits a tensile strength (at .2% proof stress) of between 90 and 133 t.s.i., depending on the relative composition. The material differs most strikingly from other high strength steel alloys in that it is hardened by a low temperature heat treatment, which 'marages' the martensite by causing a precipitation of intermetallic compounds. This treatment causes negligible distortion so that the rotor can be machined before hardening it.

In the unhardened condition the steel has a hardness of around 300 Brinell, which makes machining readily possible. The particular type of steel used goes by the trade name of maraging steel 648C (Firth Brown Ltd.) and has a tensile strength (at .2% proof stress) of 125 t.s.i. It consists of Ni (18%), Co (9%), Mo (5%), Ti (0.6%), Al (0.1%), Si (.05%) and C (0.2%). The full strength of the material was developed by keeping it for 4 hours in an inert atmosphere at 460°C.

6.3 Machining of the Rotor.

The rotor was machined in two stages. After eliminating the bulk of the material on a conventional lathe, the top surface and the rim were shaped on a profile lathe using a pattern made of bakelite. The negative of the surface was also put into a brass disc,

* The help received from the Vacuum Melting Dept. Of Firth Brown Ltd., who put several slabs of the material at our disposal, is gratefully acknowledged.

which then served as a tool to hold the rotor while the lower surface was shaped. A set of grooves had been cut into the brass disc so that the rotor could be araldited into position during the machining process and later removed again. The brass block also served conveniently to hold the rotor while the absorber skirt was ream-fitted.

The finished rotor was tested ultrasonically for structural weaknesses. This was done by submerging it into a tank of water to couple it with the ultrasonic antenna and receiver. No marked change in the echo times could be detected.

7. Acceleration of the Rotor.

Accelerating the rotor turned out to be a major problem. It was not possible to accelerate it mechanically as the axis of the rotor was not accessible, so that the only alternative was to accelerate the rotor using an externally rotating magnetic field. Unfortunately, the acceleration rate with the big rotor was very small (4 cps per minute) and was also limited by the eddy current heating, so that it became necessary to optimize a number of parameters.

7.1 General Considerations.

The basic acceleration mechanism resulting from the rotating magnetic field can be understood by considering a conducting ferromagnetic body regular in shape, like for instance a sphere, so that the magnetic flux density in the body is approximately uniform. A torque in the direction of the rotating field will then result, because of the interaction between the induced eddy currents in the body and the applied field.

Choosing a set of Cartesian coordinates, as shown in Figure 5.9, with the z-axis parallel to the axis of rotation of the magnetic field and ω_B the angular velocity thereof, we have

$$\underline{B} = \hat{i}B_x + \hat{j}B_y = \hat{i}B\cos\omega_B t + \hat{j}B\sin\omega_B t$$

$$\text{and} \quad \dot{\underline{B}} = -\hat{i}\omega_B B_y + \hat{j}\omega_B B_x$$

Applying Faraday's law,

$$\underline{V} \times \underline{E} = -\frac{\partial \underline{B}}{\partial t}$$

one finds then that the induced electro-motive forces will be in the plane parallel to both \underline{B} and $\underline{\omega}_B$. In fact, considering an annular ring in the plane parallel to \underline{B} and rotating with the magnetic field, the electric field will be given by

$$\underline{E} = \frac{1}{2}\omega_B B(-\hat{i}z + \hat{k}x) = \rho \underline{J}$$

where ρ is the resistivity of the material and \underline{J} the current density in the annulus.

The resulting torque on a small element in this annular ring will be

$$\underline{\tau}_{EC} = \underline{r} \times (id \underline{\ell} \times \underline{B})$$

$$\text{so that} \quad |\underline{\tau}_{EC}| \propto \omega_B B^2$$

This torque will act on the element so as to accelerate it in the direction of the rotating field. In fact, it has been shown that the torque acting on the element when the magnetic

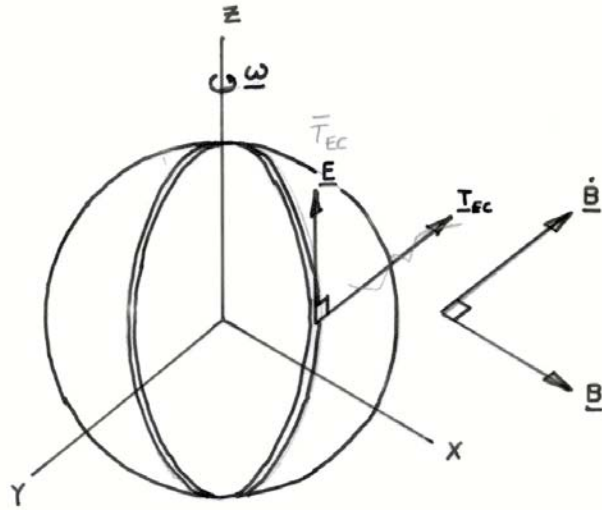


FIGURE 5.9

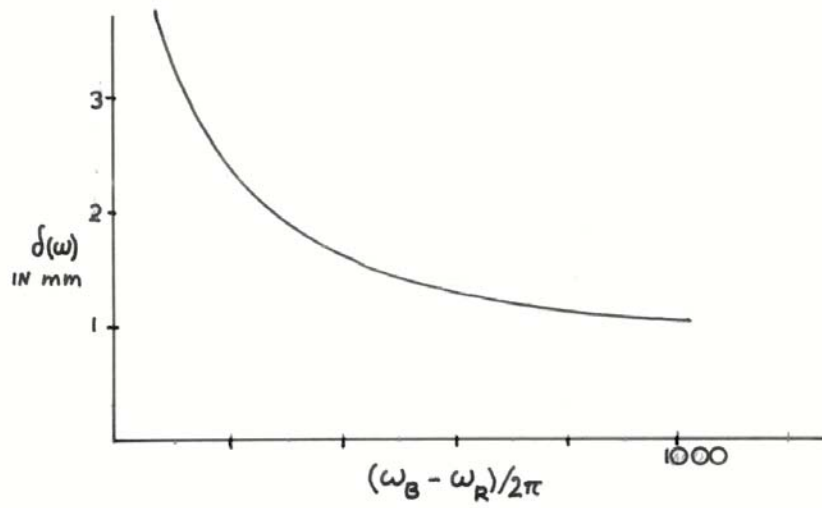


FIGURE 5.10

field is stationary but the body rotating with angular velocity $\omega_R = -\omega_B$ is the same as above, and in general depends on the difference of the two frequencies (Jonas, 1960).

Above considerations hold only when the magnetic flux density is uniform throughout the conducting body. For high frequencies this is not the case as the magnetic field will only penetrate a finite depth given by

$$\delta = \left(\frac{2r}{\mu_0 \mu (\omega_B - \omega_R)} \right)^{1/2}$$

so that when δ is smaller than the 'average' radius r of the body the eddy current torque will be effective only over the skin layer and the total torque will be

$$T_{EC} \propto (\omega_B - \omega_R) B^2 \text{ for } \delta \ll r$$

$$T_{EC} \propto (\omega_B - \omega_R)^{1/2} B^2 \text{ for } \delta \sim r$$

Figure 5.10 shows that for maraging steel the penetration depth is quite small, for $(\omega_B - \omega_R)/2\pi = 100$ cps it is 3.5 mm so that the $(\omega_B - \omega_R)^{1/2}$ dependence will dominate throughout the frequency range.

For a ferromagnetic material an additional torque will act on the body arising from the rotational hysteresis, as the induced magnetization in the material lags behind the applied rotational field. When the applied field is constant and the magnetic

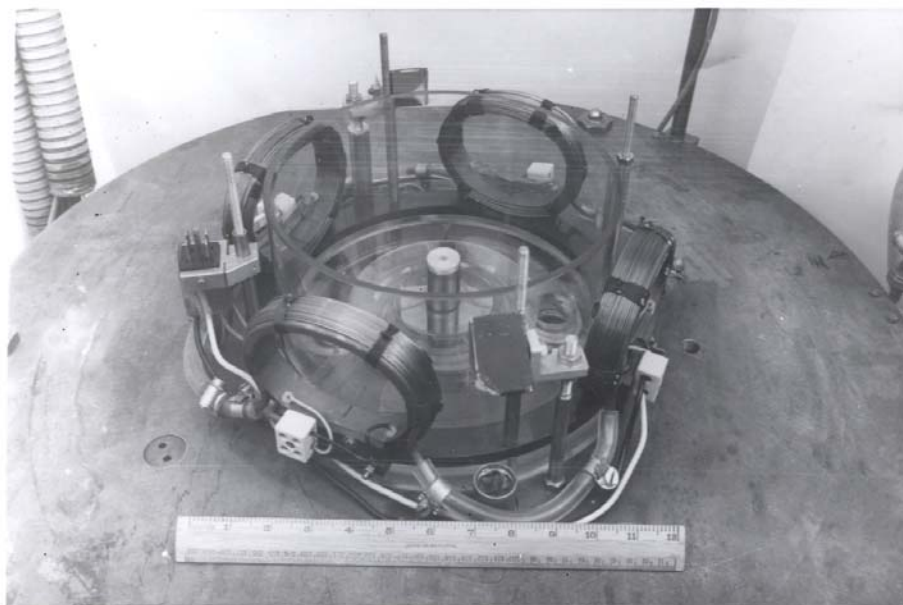


PLATE 5.4. Vacuum chamber with proportional counter and small accelerating coils.

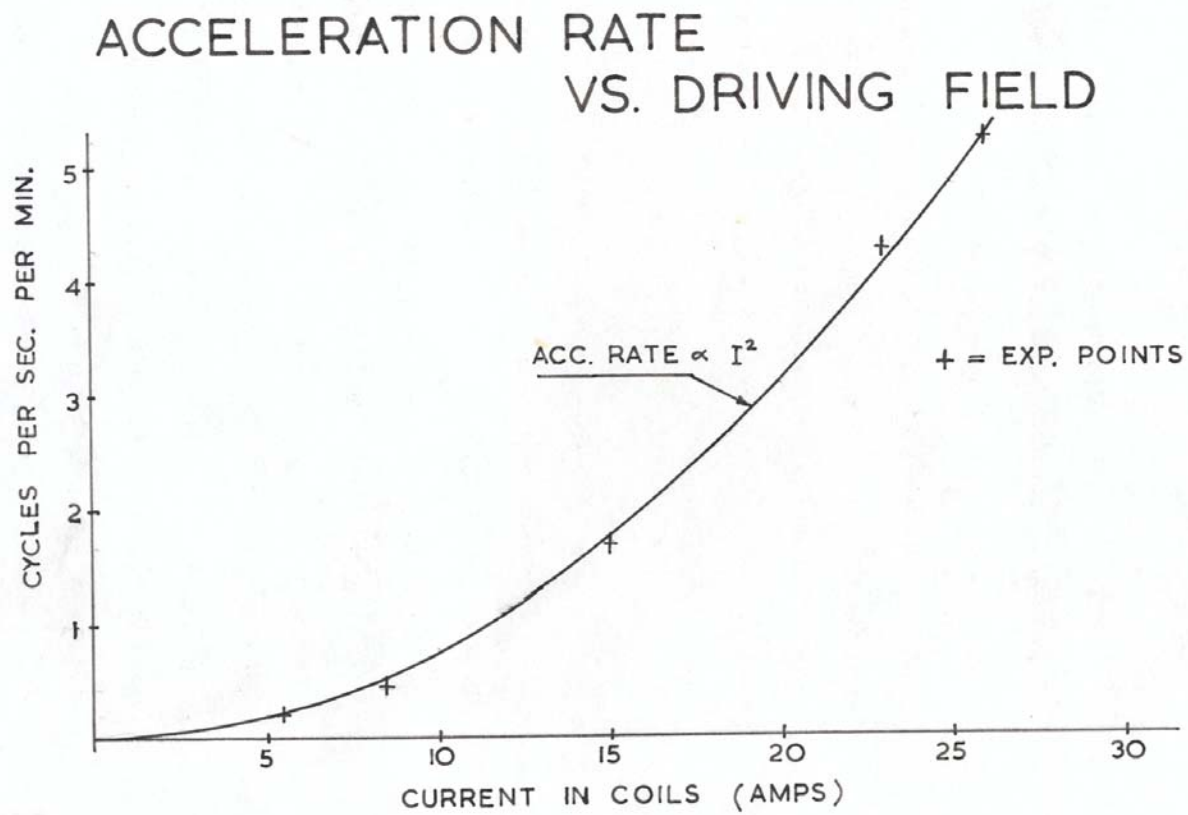


FIGURE 5.11

properties of the material isotropic the hysteresis torque per unit volume can be described by (Bozorth, 1951; Jonas, 1960)

$$\tau_H \propto B^2 \sin \theta$$

where θ is the hysteresis angle between the field strength and the intensity of magnetization. For the frequencies we are concerned with θ will stay relatively constant (Evershed and Vignoies Ltd., London, Data sheet 5A section 3) and for low flux densities, as used here, will be negligible.

7.2 Experimental Considerations.

Rotating magnetic fields have been employed in this laboratory to accelerate smaller rotors (Marshall et al., 1948) and the same basic set-up is used in the present experiment. Two generators rated at 500 watts each and adjusted to be in quadrature supplied the power to two sets of coils. The first set of coils (see Plate 5.4), each coil consisting of 200 turns of 18 SWG copper wire, was built to investigate the acceleration rates for the big rotor. The rates were disappointingly small but were, as expected, proportional to B^2 at constant $(\omega_B - \omega_R)$ (see Figure 5.11).

During an actual rotor run, however, it was found that the acceleration rate decreased much more quickly than could be accounted for by the above arguments. Figure 5.12 shows the expected rate and that found with the first set of coils. The decrease in the acceleration rate was so marked that in fact one could not have accelerated beyond 400 cps using a driving frequency $f_B = 950$ cps or beyond about 600 cps using $f_B = 2500$ cps.

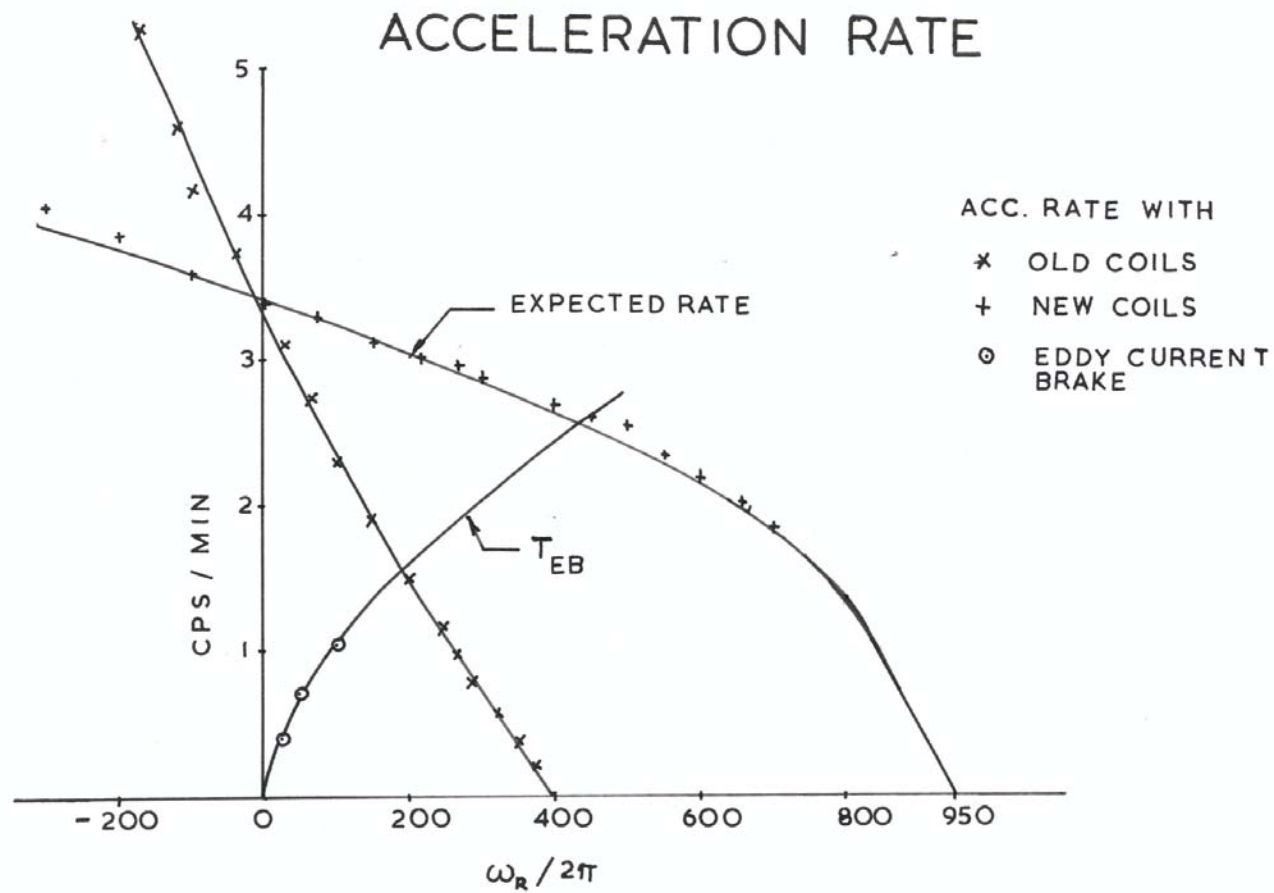


FIGURE 5.12

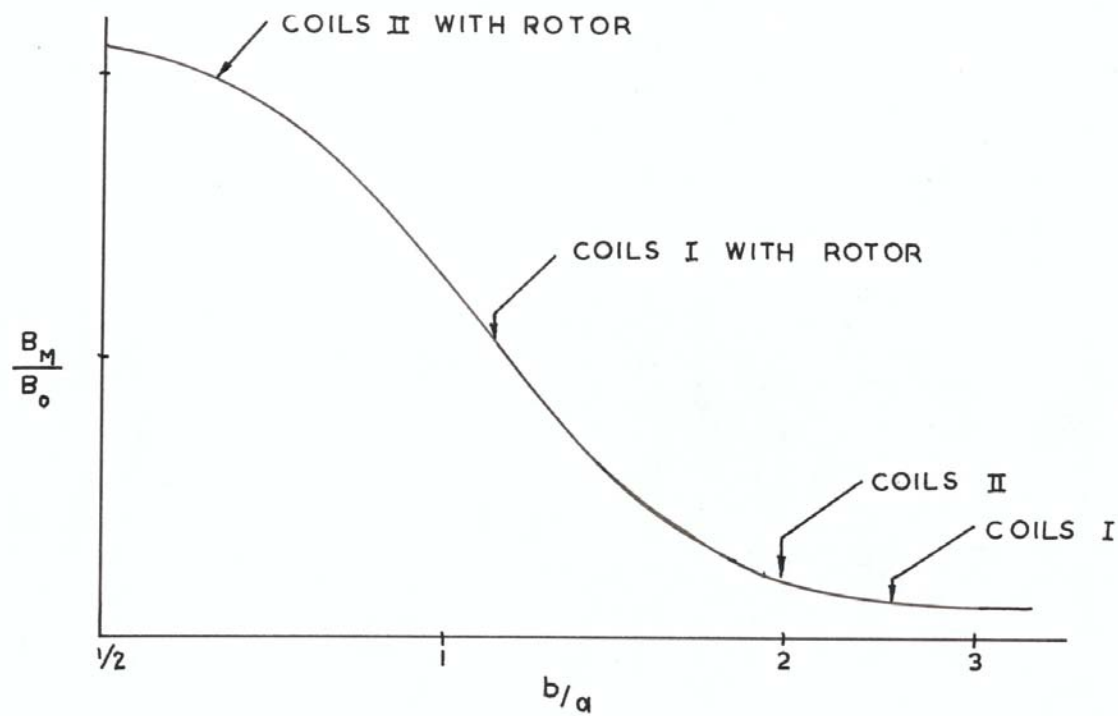


FIGURE 5.13

This rapid decrease in the torque is explained by the nonuniformity of the rotating magnetic field. If one considers two coils of radius a in a Helmholtz geometry with distance of separation $2b$, then the magnetic field B_m halfway between the two coils will be as shown in Figure 5.13. Separating the coils decreases B_m rapidly relative to the field B_0 at the center of one of the coils. The ratio B_m/B_0 gives essentially the fraction of the field penetrating both coils, i.e., the 'uniform field.' Only this uniform component of the field will contribute to the rotating field, whereas the non-uniform component B_n will appear as stationary in the laboratory frame. It will hence set up a braking torque

$$T_{EB} \propto \omega_R^{\frac{1}{2}} B_n^2$$

which is directed opposite to ω_R and increases with $\omega_R^{\frac{1}{2}}$. That this explanation does account for the discrepancy in the acceleration rate has been verified by measuring the braking torque for various rotor frequencies by disconnecting one set of coils to eliminate the rotating magnetic field. The curve marked T_{EB} (in Figure 5.12) has been obtained by extrapolating the low frequency dependence to higher frequencies, which does account for the limiting of the acceleration rate at $f_R = 400$ cps.

In order to obtain a more uniform magnetic field, another more ideal set of coils was built (see Plate 5.5) that was also matched to the generators to obtain maximum power output. The power generators had an internal impedance of $Z_G = 25$ at 950 cps and a power output of $I_g = 4.4$ amps (RMS) at $V_g = 110$ volts (RMS). The new set of coils, with a geometry as shown in figure 5.13, were wound with 520 turns of 18 SWG copper wire and used in a series resonance circuit. This turned out to be an unfortunate

choice as the voltage across the coils was ~900 volts, which the coils could not withstand for long. A faint smell of ozone detected during the acceleration substantiated this view.

Current amplification, using a parallel resonance circuit with low impedance coils was found to be preferable. The optimum impedance of the coils is given by

$$Z_c = \frac{R_1 + j^\omega L_1}{2} = \frac{Z_g}{Q} \text{ where } R_1 \text{ and } L_1 \text{ are the resistance and the inductance of the}$$

individual coils connected in parallel. The quality factor Q of the above coils was found to be 8.2 for $f_B = 950$ cps. It was measured with a Wayne Kerr Universal Bridge so as to include the eddy current losses in the coils. As the quality factor can be considered to be constant for coils having the same geometry and volume of copper, the values of R_1 and L_1 for a parallel resonance circuit can be readily found.

The final coils were wound with 72 turns of .2" x .08" copper strips giving an inductance of .26 mh.

After installing the coils, the quality factor actually decreased to 5 because of losses in the supply cables and the steel safety barricades around the coils. These losses could not be reduced because the supply cables had already been made as short as possible and the inner of the two steel barricades removed.

The acceleration rate using the new coils did follow the expected theoretical curve and improved the overall efficiency of the acceleration system even though initially the acceleration rate was not larger than before. It took about 12 hours to accelerate the rotor to 700 cps compared with the 24 hours it took to reach 450 cps when using the small coils.

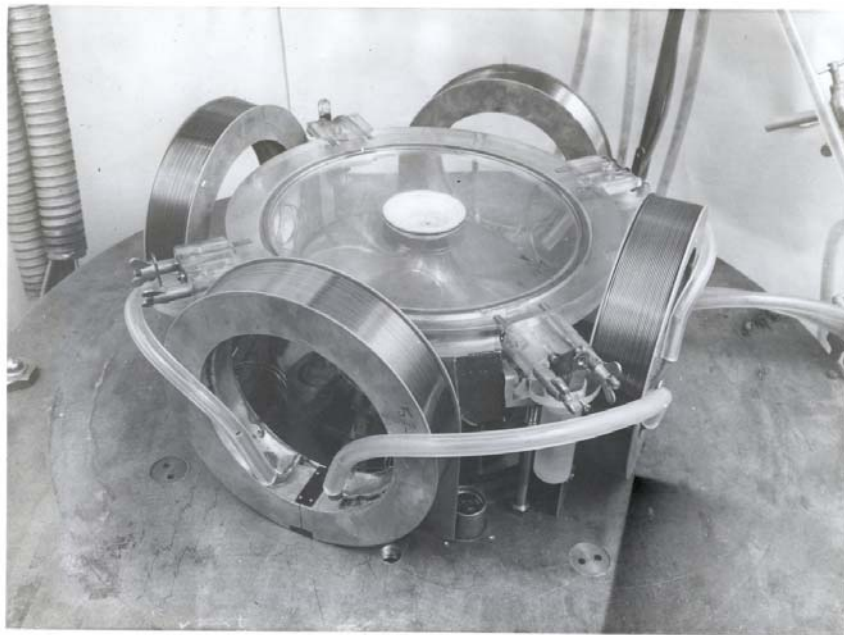


PLATE 5.5. Vacuum chamber showing the damping assembly and big accelerating coils.

7.3 Eddy Current Heating.

The acceleration rate was then not so much limited by the power output of the generators as by the eddy current heating in the rotor. The absorber material, sodium ferrocyanide in araldite, would have decomposed at 120°C and this set the limit on the allowable rotor temperatures.

The power dissipated in the rotor can be found by

$$P = T_{EC} |(\underline{\omega}_B - \underline{\omega}_R)|$$

assuming that no higher harmonics in frequency are present.

The heating of the rotor is given by

$$H_T = \frac{I\alpha |(\omega_B - \omega_R)|}{CM}$$
$$= .96^\circ C/\text{min} \quad \text{for } \omega_R = 0$$

where I is the rotational inertia of the rotor ($1.07 \times 10^{-2} \text{ kg.m}^2$) α is the frequency dependent rate of acceleration (3.6 cps/min at $\omega_R = 0$), M the mass of the rotor (2.7 kg) and C is the specific heat of iron equal to $1.2 \times 10^2 \text{ cal/kg } ^\circ\text{C}$.

The figure agrees well with the experimentally determined value of $1^\circ\text{C}/\text{min}$ for $f_B = 950 \text{ cps}$.

In order to keep the temperature of the rotor below the tolerable limit, alternate cycles of acceleration and cooling had to be used. Figure 5.14 shows the rate of cooling for two different pressures from which the relative length of each cycle can be deduced.

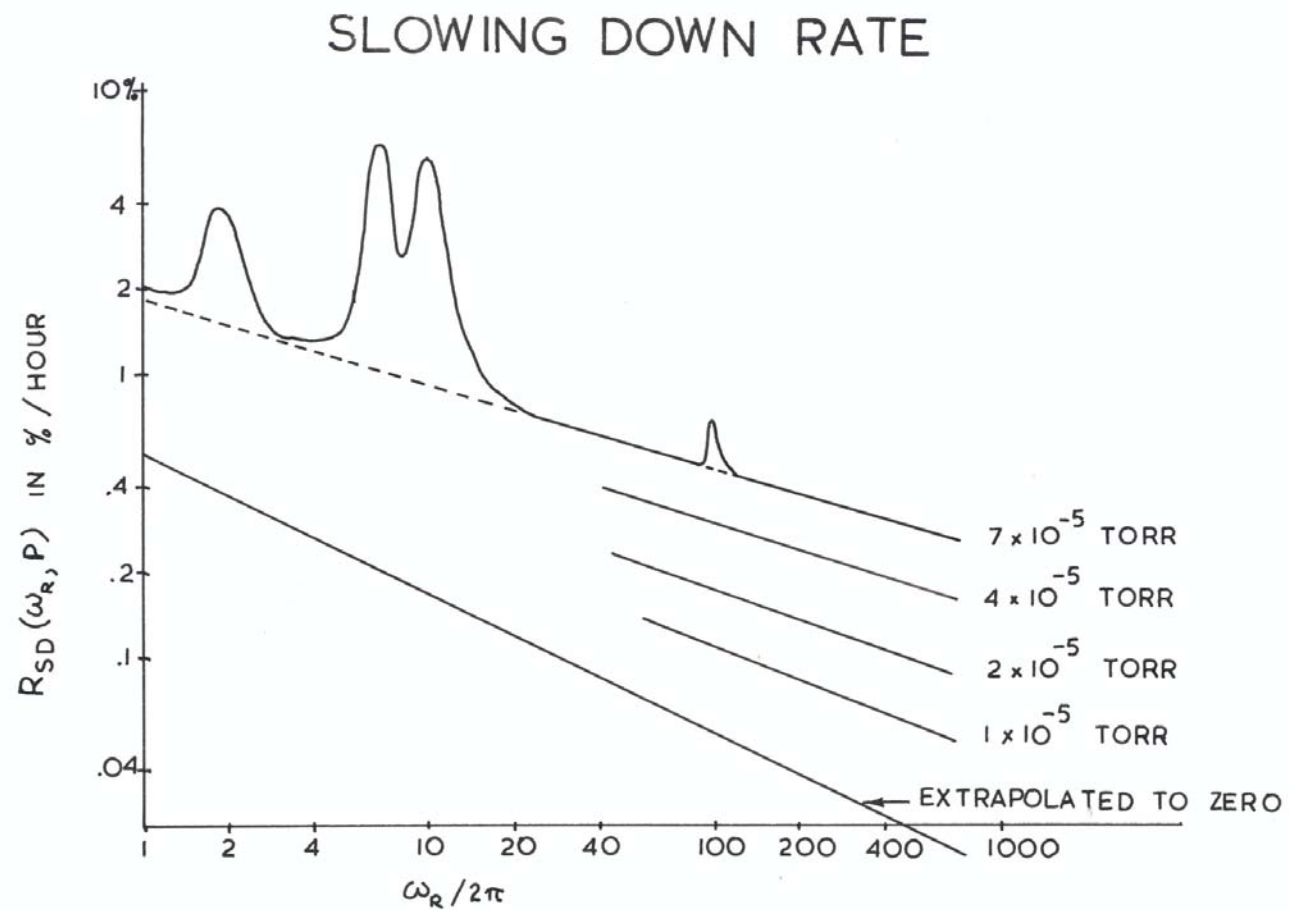


FIGURE 5.15

For f_R equal to 0, 200, 500, and 700 cps, the cooling cycle has to be 1.7, 1.2, .56, and .23 times the acceleration cycle respectively, so that the total acceleration time would be increased very little by increasing the acceleration rate.

Unfortunately no direct method was available to measure the rotor temperature. Usually a deterioration of the vacuum gave a rough indication of the rotor temperature, but as the vacuum improved toward the end of a long run, even this method was not very reliable.

8. Slowing-down Rate of the Rotor.

Before the rotor was tested at high speed, the main fear was that it might exhibit some resonances at higher velocities which could make it unstable. As the slowing down rate of the rotor in a vacuum did give a good indication of the stability of the suspension system and the general vibration level, it was monitored over the whole frequency range. The slowing down rate is shown in Figure 5.15 as a function of rotor frequency and vacuum pressure.

The resonances at 2, 7 and 10 cps can be explained by the action of the damped pendulum. The lower resonance is caused by the motion of the rotor about its point of suspension. The length of this effective pendulum, deduced from the period, is 6.2 cm corresponding to the distance between the center of mass of the rotor and the suspension point at the core. The two higher resonances are representative of the vibrational frequencies of the leaf springs along the two axes, and the resonance at 100 cps caused by the interaction of the vertical and the horizontal motion of the rotor, was eliminated by

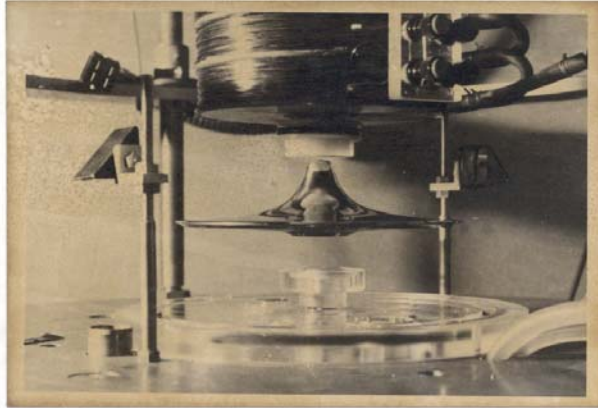


PLATE 5.6. **Rotor as suspended**

the stabilized power supply. No other large resonances were observed, even though some effect was expected at half synchronous speed.

Two features are brought out by Figure 5.15:

- i) the slowing down rate $R_{sd}(P)$ is proportional to the residual vacuum pressure P ,
and

- ii) $R_{sd}(\omega_R) \propto \omega_R^{\frac{1}{2}}$ for constant P , as given by the slope of $R_{sd}(\omega_R)$.

The remanent slowing down rate decreased with increasing rotor speed and can be attributed to an imbalance in the rotor. Monitoring the control signal of the suspension current a ripple was observed, which had the same frequency as that of the rotor. This also indicated that the rotor was not running true, i.e., that the center of mass of the rotor did not fall on the axis of rotation. It can be assumed, however, for the later analysis, that the center of mass of the rotor does prescribe a circular motion about the axis of rotation and that the radius of this circular path decreases with increasing rotor frequency.

Some attempts were made to obtain a vacuum of around 10^{-6} torr limited only by the pumping rate of the diffusion pump (150 l/sec), but the best vacuum actually achieved was 1.6×10^{-5} torr. This was probably caused by the outgassing of the perspex parts of the vacuum chamber, but polishing the perspex and covering it with Apiezon grease did not improve the vacuum. It was found, however, that the slowing down rates were quite acceptable and required only the occasional accelerating burst every 90 minutes to keep the rotor at speed.

9. Safety Devices.

Several safety features had to be incorporated to protect against a high speed rotor crash, and to dissipate the kinetic energy of the rotor of $\sim 10^5$ joules. A system of concentric steel barriers guarded against fragments from a disintegrating rotor and also served to take up some of the angular momentum. For that reason the inner steel barrier, which was 7" high and had a wall thickness of $1\frac{1}{4}$ ", was mounted on ball bearings and also lined with plasticene to soften the impact.

The outer steel barrier was $8\frac{1}{2}$ " high and consisted of two $\frac{3}{4}$ " concentric steel cylinders that were bonded together by a lead filling as an added radiation shield. Both steel barriers could be demounted by a hoist to allow more working space.

A wooden barricade surrounded the whole structure to a height of six feet and provided further protection. It was constructed of 5" x 10" railway sleepers and consisted of two movable L-shaped sections. The whole assembly was kept in an enclosure separate from the rest of the laboratory with the rotor operation controlled remotely.

Additional safety features guarded against an overheating of the diffusion pump and protected it against a failure of the backing pump.

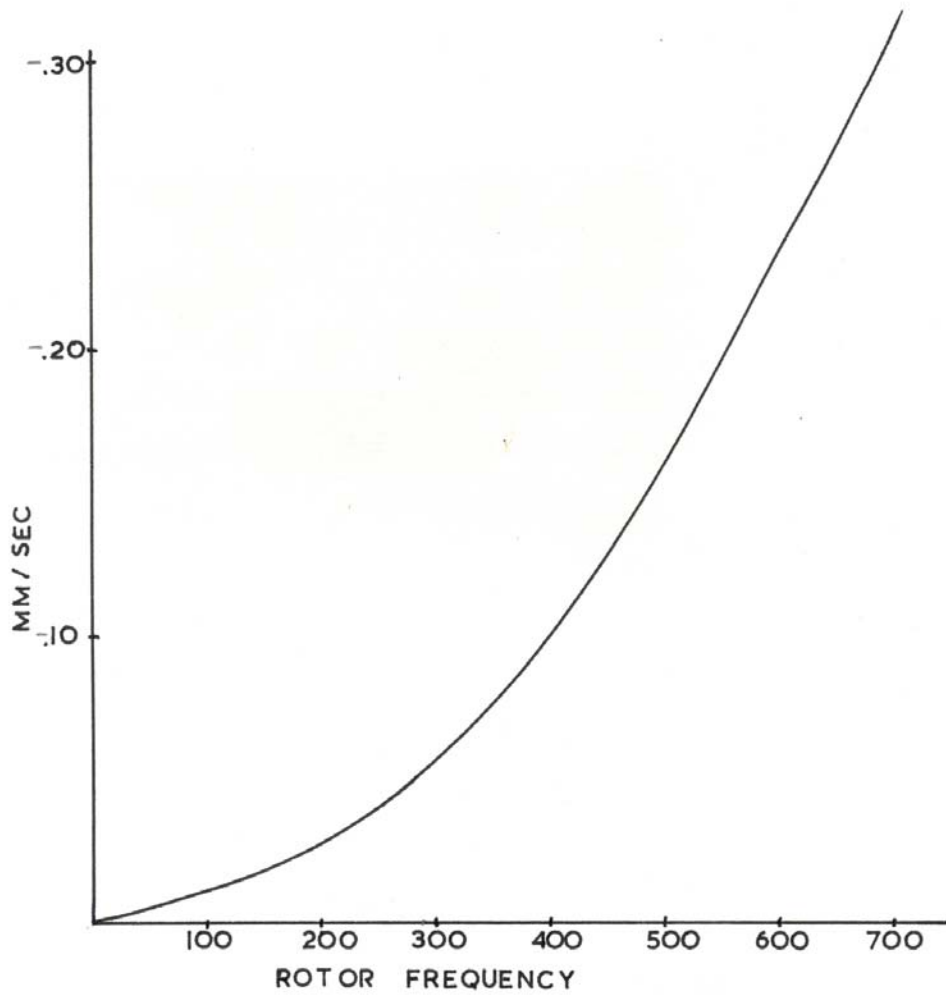


FIGURE 6.1